DOI 10.1007/s10946-024-10207-4
Journal of Russian Laser Research, Volume 45, Number 2, March, 2024

EFFECT OF PRELIMINARY HEAT TREATMENT ON THE FORMATION OF STRUCTURE AND RESIDUAL STRESSES IN THE AMg6 ALLOY AT LASER SHOCK PEENING WITHOUT COATING

I. A. Bakulin, S. I. Kuznetsov, A. S. Panin,* E. Yu. Tarasova, S. I. Yaresko, and V. A. Novikov

Samara Branch of the P.N. Lebedev Physical Institute, Russian Academy of Sciences 221 Novo-Sadovaya Str., Samara 443011, Russia

*Corresponding author e-mail: anton@fian.smr.ru

Abstract

We consider the effect of laser shock peening without coating (LSPwC) on the structure and stress state of the AMg6 Aluminum alloy with a thickness from 4 to 14 mm before and after preliminary thermal annealing. The roughness parameters R_a and R_z after LSPwC are determined. The magnitude, depth, and profile of compressive residual stresses (CRS) are found to depend on the thickness of the material and preliminary heat treatment. The layer-by-layer X-ray diffraction analysis shows a correlation between the parameters of the crystal structure and the profile of residual stresses for the processed samples. We find homological distortions of the crystal lattice in the CRS zone and observe the formation of significant (up to −100 MPa) residual stresses on the unprocessed side of the samples. Also, we determine the surface CRS magnitudes for double unilateral and bilateral processing.

Keywords: laser shock peening without coating, plastic deformation, dislocations, residual stresses, annealing, Aluminum alloys.

1. Introduction

Being an alternative to traditional methods of hardening the surface of structural materials by plastic deformation, in particular, shot peening and ultrasonic impact treatment, laser shock peening (LSP) has found wide application in various industries [1, 2].

One type of the LSP is laser shock peening without coating (LSPwC) [3]. The promise of this method is that the processing can be carried out without any preliminary surface preparation or sacrificial coating, since with LSPwC the hardening effect can be achieved with a pulse energy smaller than 1 J and a laser spot size of 1 – 2 mm. This approach makes it possible to use relatively cheap low-power laser systems with a higher pulse repetition rate of 10 – 100 Hz [4, 5].

At LSPwC, it is necessary to evaporate part of the material being processed to induce near-surface plasma, which leads to increase in the surface roughness [6, 7]. However, the absence of a "sacrificial" coating is also an advantage, since its application requires preliminary preparation of the surface to be processed and, moreover, the shape of the products does not always allow effective application of such coatings. In addition, the lower energy of laser pulses makes it possible to transmit them through optical fibers and process objects immersed in water with a high processing depth [8].

Manuscript submitted by the authors in English on February 27, 2024.

In recent years, the effect of LSPwC on the structural and performance characteristics of structural materials has been studied. First of all, attention was paid to the formation of residual stresses and the macrostructure of the surface after laser processing [6,7,9,10]. The effect of LSPwC on the microstructure of the processed material was studied [11, 12]. It has been shown that LSPwC leads to increase in the wear resistance [13], fatigue strength [14, 15], and corrosion resistance [16, 17].

However, despite long-term research and extensive efforts, there is still no complete understanding of the effect of some important factors on the processing result. For example, there is no systematic experimental data on the effect of the thickness of the processed material and its preliminary heat treatment (annealing, hardening, etc.) on the depth and profile of residual stresses.

Previously, we obtained experimental data on the effect of low-energy laser shock peening on the structure and residual macrostresses for the AMg6 alloy, both with and without an absorbing coating [18, 19]. The choice of AMg6 as an object of study is stipulated by its wide use in technology, as well as the lack of studies on laser shock peening of this alloy.

The goal of the present study is to provide a comparative analysis of the effect of low-energy laser shock peening on the structure and residual macrostresses in the AMg6 alloy of various thickness in the as-received state and after recrystallization thermal annealing.

2. Materials and Methods

2.1. Experimental Samples and Processing Technique

The materials under study were flat round samples of the AMg6 alloy with a diameter of 25 mm and the thickness H equal to 4, 6, 8, 10, and 14 mm cut from a rod of a polycrystalline industrial alloy. Residual stresses in the original AMg6 are close to zero. According to the quality certificate, the alloy contains Al as the base and 6.7 wt.% of Mg, 0.69 wt.% of Mn, 0.26 wt.% of Fe, 0.16 wt.% of Si, 0.049 wt.% of Ti, 0.011 wt.% of Zn, 0.004 wt.% of Cu, and 0.0025 wt.% of Be.

To study the effect of the preliminary heat treatment on the microstructure and residual macrostresses after LSPwC, samples are used in the as-received condition (hereinafter referred to as original or not annealed samples) and after annealing in an SNOL electric furnace at temperature $T = 335°$C for 2 h (hereinafter referred to as annealed samples).

The radiation source is a solid-state YAG : Nd laser with the wavelength $\lambda = 0.532$ μm, pulse duration $\tau = 10$ ns, pulse energy $E = 0.35$ J, and a pulse repetition rate of 1 Hz.

Uncoated samples are processed under a 60 mm thick layer of flowing distilled water with a stepwise displacement ℓ equal to 0.25 and 0.5 mm. The pulse density N is 2,000 and 400 pulses/cm^2, corresponding to the displacement. The processed samples are moved along two coordinates x and y, and the scanning pattern is a zigzag; see Fig. 1.

The power density $q = 4.4$, 2, and 1.1 GW/cm^2 is varied by changing the diameter of the focused beam $d = 1$, 1.5 and 2 mm, respectively, using a lens with a focal length of 100 mm. The dimensions of the processed region are 15×15 mm. To clarify some results, a region of 5×5 mm is processed. To analyze the roughness, we also carry out two- and three-cycle surface processing, either in the same direction or in the perpendicular direction (with the sample rotated by 90°).

2.2. Analysis of Structure and Residual Stresses

Metallographic specimens are prepared by sequential grinding and polishing on felt fabric moistened with a suspension of Chromium oxide or a diamond suspension. After that electrolytic polishing is carried out for 1 – 2 min. At the final stage, the sample is etched with the Keller's reagent to identify grain boundaries.

We determine surface roughness before and after LSPwC (along and across the scanning direction) using a TR200 contact profilometer. We study the microstructure of the materials under study using a Neophot 30 optical microscope and a Jeol scanning electron microscope with an elemental analysis unit. Microhardness is measured using a PMT-3 microhardness tester. X-ray structural analysis is carried out on a DRON-3 X-ray diffractometer with Cu K_α radiation. We study the depth distribution of residual stresses with layer-by-layer removal of the material by electrolytic polishing. The macrostresses σ_x and σ_y along and across the laser scanning direction (Fig. 1) are determined from the shift of the (511) diffraction peak, using the $\sin^2\psi$ technique. The methods for preparing samples and analyzing the structure and residual stresses are described in more detail in [18, 19].

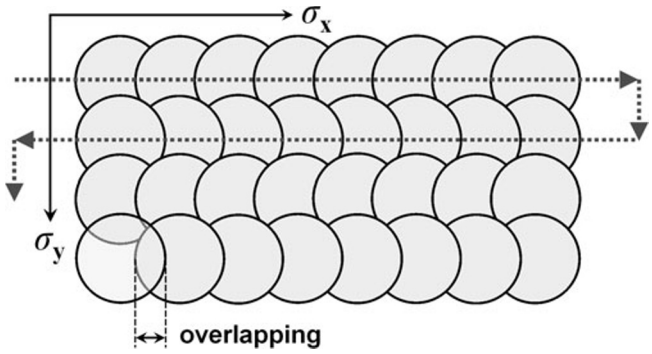

Fig. 1. Scanning scheme for LSPwC.

3. Results and Discussion

3.1. Surface Structure

Based on the results of measuring the weight of the samples on analytical balances before and after LSPwC, under the assumption that mass loss occurs due to evaporation, we calculate the thickness of the evaporated layer at $E \approx 0.3$ J on the surface, $d = 1$ mm, and $N = 2,000$ pulses/cm^2. The calculated thickness equal to 15.5 μm is in good agreement with the result of profilometry of the border between the unprocessed and processed areas, which showed a height difference of 15 – 16 μm. According to the estimates, about 25% of the incident radiation energy is spent on removing the surface layer.

Table 1. Roughness Parameters of AMg6 after LSPwC.

	q_1, ℓ_1 original		q_1, ℓ_2 original		q_1, ℓ_2 annealed		q_2, ℓ_1 annealed		q_2, ℓ_2 annealed		q_3, ℓ_2 annealed	
	x	y	x	y	x	y	x	y	x	y	x	y
R_a, μm	2.1	2.5	2.4	2.5	2.9	2.4	1.2	1.2	2.3	2.5	1.4	1.8
R_z, μm	13.7	14.6	16.3	17.1	16.4	14.3	7.9	8.3	14.8	16.2	9.0	11.3

In Table 1, we show the average results of measuring the surface roughness of the samples processed with different exposure parameters. The arithmetic mean deviation R_a of the profile and the height R_z of irregularities along (x axis) and across (y axis) the scanning direction are estimated.

In Table 1, values of the parameters read $q_1 = 4.4$ GW/cm^2, $q_2 = 2$ GW/cm^2, and $q_3 = 1.1$ GW/cm^2, while stepwise displacements are $\ell_1 = 0.25$ mm and $\ell_2 = 0.5$ mm. The roughnesses of the samples before LSPwC are in the range of $R_a = 0.4\,\mu\text{m} - 1.1\,\mu\text{m}$ and $R_z = 2.9\,\mu\text{m} - 6.3\,\mu\text{m}$.

From the results obtained it follows that after LSPwC the roughness parameters sometimes increase by 4 – 5 times. In this case, the roughness after processing is almost independent of the roughness before processing. The increase in both R_a and R_z depends on the power density and processing step, which is also noted in the literature [20], and is almost independent of the preliminary thermal treatment of the samples. Since the change in the surface profile is mainly due to material ablation, the roughness after LSPwC is largely determined by the power density. Repeated processing does not lead to noticeable changes in the roughness.

3.2. Effect of LSPwC on the AMg6 Microstructure

Compared to sheet AMg6 considered in [18, 19], the material under study exhibits a pronounced banded structure of grains and a line arrangement of insoluble compounds along the axis of the original rod. According to the elemental analysis, these compounds most often include Mg, Mn, and Fe or Mg, Mn, Si, and Fe, in addition to Al; see Fig. 2.

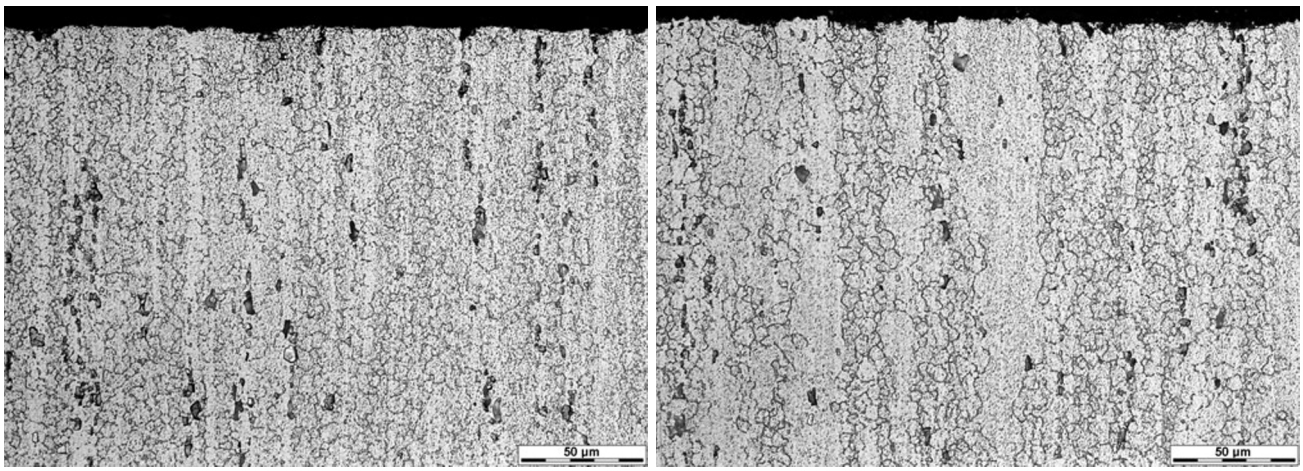

Fig. 2. View of transverse sections of AMg6 before LSPwC original (left) and annealed (right).

The grain size of the original AMg6 is mainly 3 – 10 µm, which is significantly smaller than in the sheet AMg6 used previously, where it reached 50 µm, with the grains elongated along the rolling direction. Precipitates of intermetallic phases are clearly visible in the body of the grain. Judging by the elemental analysis, these are mainly intermetallic compounds of the Al – Mg system. After annealing, the grains become more rounded and somewhat enlarged, but their size, on average, remains within 10 µm.

At LSPwC, a thin layer of molten material is formed on the surface of the laser irradiation zone. The appearance and structure of the surface after processing do not differ from those presented in [19]. In addition, under the upper recrystallized layer with a thickness of about 10 µm, the other layer with a changed structure is observed, which is formed as a result of severe plastic deformation. The total thickness of these layers can reach 70 µm being depended on the processing parameters. Except for the surface layer, no noticeable differences between the microstructure of unprocessed and processed samples can be detected by either optical or scanning electron microscopy.

The microhardness of the samples before and after annealing differs slightly and is in the range of 75 – 80 $HV_{0.05}$. Laser shock peening, as in [19], leads to a very noticeable increase in microhardness up to 100 $HV_{0.05}$ at the maximum with a significant spread of values over depth. The observed depth of increase in microhardness, after processing at $q = 4.4$ GW/cm^2 and $N = 2000$ pulses/cm^2, is 800 μm for the non-annealed material and 400 μm for the annealed material.

Structural differences between the annealed and original AMg6 are clearly visible at X-ray diffraction analysis. First, the intensity ratio I_{hkl} of the lines in the X-ray diffraction patterns indicates the presence of a pronounced texture of the original alloy that changes somewhat after annealing, which is expressed in a change in the intensity of diffraction lines; see Fig. 3. So, if before annealing $I_{111}/I_{200} \approx 0.9$, then after annealing $I_{111}/I_{200} \approx 1.1$. In this case, the preferential orientation of the {111} and {100} crystallographic planes parallel to the processed surface (perpendicular to the axis of the original rod) is maintained. Second, after annealing, the width of the diffraction lines decreases, which indicates a decrease of the dislocation density ρ and microstrains ε, as well as an increase in the apparent size D of coherent scattering regions (CSR).

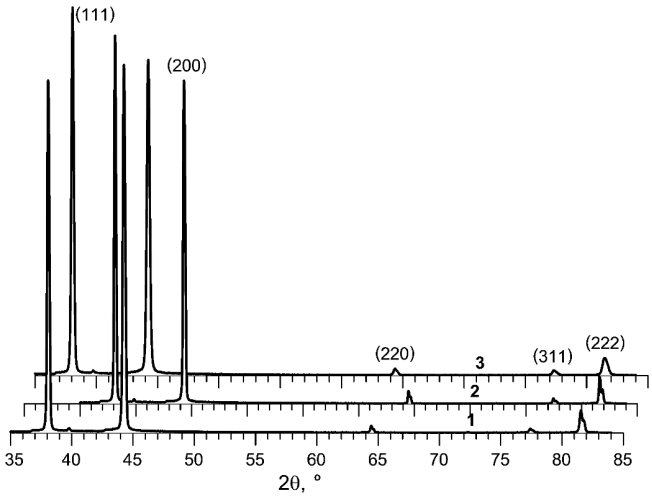

Fig. 3. Fragments of X-ray diffraction patterns for AMg6 samples; here, the original sample (1), original sample after LSPwC (2), and annealed sample (3).

We determine the dislocation density and other structural characteristics by analyzing the profile of the (200) X-ray diffraction line since, in FCC lattices, structural defects are best manifested in changes in the profile of this line. For this purpose, we approximate the experimental and instrumental lines by asymmetric pseudo-Voigt functions; the calculation method is described in [18, 19]. Let us emphasize that, in the case at hand, we consider estimates of structural characteristics.

According to the calculations, we have $D = 120 - 130$ nm, $\varepsilon \approx 0.0009$, and dislocation density $\rho \approx 8 \cdot 10^{13} - 8.8 \cdot 10^{13}$ m^{-2} on the surface of the unprocessed, non-annealed material. For the annealed material, we have $D > 300$ nm, $\varepsilon \approx 0.0005$, and dislocation density $\rho < 10^{13}$ m^{-2}.

The structural characteristics of the processed samples have a clear dependence on the radiation power density and the number of repeated processing cycles. So, at $q = 4.4$ GW/cm^2 and $N = 2000$ pulses/cm^2, the minimum value equal to $D \approx 33$ nm, the maximum value equal to $\varepsilon \approx 0.002$, and the maximum dislocation density $\rho \approx 7.3 \cdot 10^{14}$ m^{-2} are achieved on the surface (after etching off the oxidized layer) with double processing. In Fig. 4, we show the dependence of the dislocation density on depth for non-annealed and annealed samples with a thickness of 4 and 14 mm after single LSPwC.

As follows from the results obtained, the maximum values of the structural characteristics with the same processing parameters are approximately the same for annealed samples with a thickness of more than 8 mm and all non-annealed samples, and in the case of a single processing cycle with $q = 4.4$ GW/cm^2 and $N = 2000$ pulses/cm^2, they are in limits: $\rho = 5.5 \cdot 10^{14} - 6.5 \cdot 10^{14}$ m^{-2}, $\varepsilon \approx 0.002$, and $D = 38 - 43$ nm. Maximum structural changes and, consequently, the most intense processes of plastic deformation in these samples occur at depths of up to 400 μm. Further, in the range of depths up to 800 – 900 μm, a smoother decrease of ρ and an increase in CSR are observed. Then a decrease of the dislocation density to the corresponding values in the untreated alloy is observed. However, as can be seen in Fig. 4, the difference

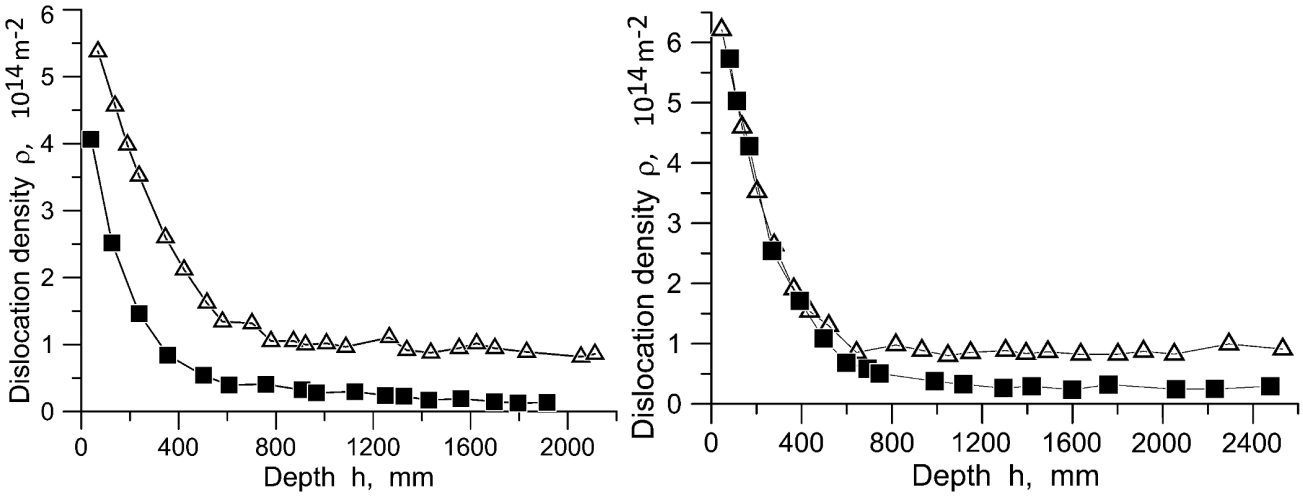

Fig. 4. Dislocation density as a function of depth; here, $q = 4.4$ GW/cm^2 and $N = 2000$ pulses/cm^2 at $H =$ 4 mm (left) and $H = 14$ mm (right) for an original (△) and annealed (■) samples.

in the structural characteristics of the annealed and non-annealed samples depends on their thickness to a depth of 600 – 700 μm. In the original samples, the dislocation density is approximately the same at the same depth, whereas in the annealed samples ρ increases at the same depth with increase in the material thickness to 8 mm. For a thickness of 14 mm, the values of the structural characteristics in the original and annealed samples are almost the same to a depth of 600 μm. The maximum values of the dislocation density and CSR for other processing parameters are given in Table 2.

3.3. Formation of Residual Macrostresses at LSPwC

In Table 2, we show the results of processing a 15×15 mm region of the initial samples with a thickness of 6 mm under various parameters of laser exposure.

Table 2. Residual Stresses on the Surface of AMg6 and Depth σ_x.

q, GW/cm^2	N, pulses/cm^2	h, μm	σ_x/σ_y, MPa	ρ, 10^{14} m^{-2}	D, μm
4.4	400	1100	$-172/-205$	4.1	47
	2000	1400	$-185\ /-239$	5.1	43
2.0	400	600	$-111\ /-117$	1.9	74
2.0	2000	1100	$-121\ /-119$	3.4	51
1.1	400	500	$-51\ /-57$	1.2	90
1.1	2000	500	$-52\ /-58$	2.1	70

The thickness of the material has a noticeable effect on the magnitude of surface residual stresses, especially in the region of $H < 8$ mm. On the surface of the original materials, with increase in H from 4 to 14 mm, σ_x changes from −170 to −200 MPa, and σ_y changes from −210 to −280 MPa, respectively. For the annealed samples, the change in σ_x with increasing thickness is from –170 MPa to –230 MPa; in

this case, σ_y changes from –210 MPa to –300 MPa. An increase in residual stresses on the surface with increasing thickness can be due to a decrease of the impact of the shock wave reflected from the back side of the sample on the plastically deformed layer [21] and homological distortions, which will be discussed below.

The size of the processed region also has some effect on the formation of residual stresses. Thus, when processing a 5×5 mm region of a 4 mm thick sample with pulses having $q = 4.4$ GW/cm^2 and $N = 2000$ pulses/cm^2, the residual stresses on the surface $\sigma_x = -176$ MPa and $\sigma_y = -192$ MPa are comparable to those obtained when processing 15×15 mm regions ($\sigma_x = -170$ MPa, $\sigma_y = -210$ MPa), whereas their depth h, which is equal to 800 and 1100 μm, respectively, is noticeably smaller than that observed when processing a larger area: 1150 and 1600 μm.

The depth distributions of the measured residual stresses in the original and annealed samples of the minimum and maximum thickness are shown in Figs. 5 and 6.

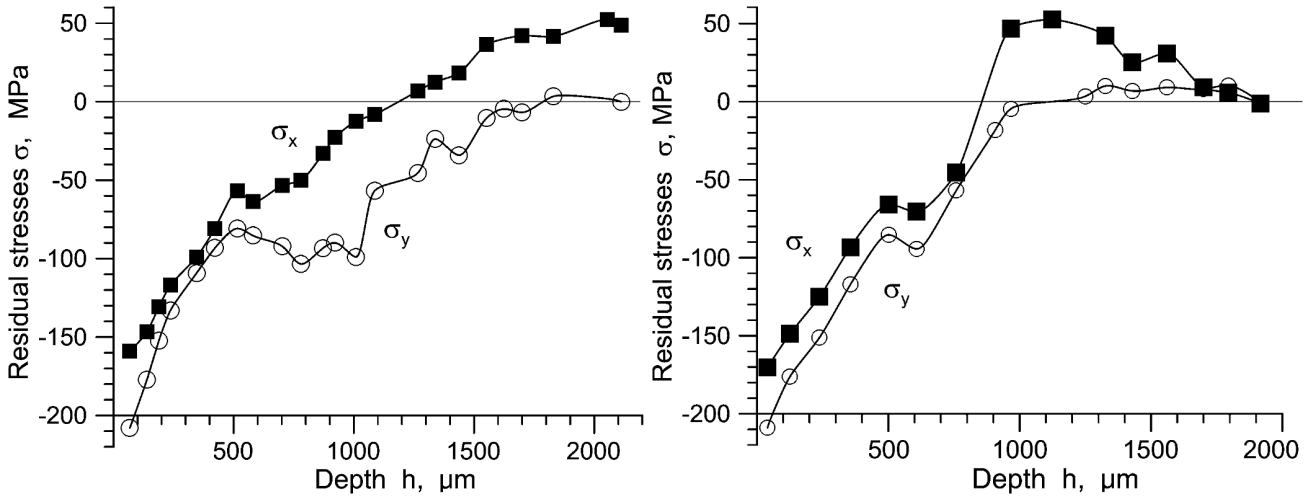

Fig. 5. Distribution of measured residual stresses σ_x (■) and σ_y (⊙) at $H = 4$ mm, $q = 4.4$ GW/cm^2, and $N = 2000$ pulses/cm^2 in original (left) and annealed (right) samples.

In the stress profile along the depth in the non-annealed samples, four regions can be distinguished: up to a depth of 400 – 450 μm with $\sigma_x < \sigma_y$ (region 1), where their graphs are approximately parallel or almost coincide; local minimum (region 2) or more often a "plateau" of stresses in the range of 450 – 800 μm with $\sigma_x \leq \sigma_y$; $\sigma_x < \sigma_y$ (region 3), while decrease of σ_x and σ_y with the depth is slower, and the ratio σ_y/σ_x is greater than in region 1; $\sigma_x > 0$ (region 4), sometimes reaching 60 MPa and $\sigma_y \approx 0$; see Figs. 5 and 6. The depth corresponding to the boundary of regions 2, 3, and 4 depends on the sample thickness. Such a behavior of the σ dependence is observed for all samples, in which the CRS depth is greater than 800 μm, although it is more pronounced for the material with a thickness of up to 8 mm.

In the annealed samples, four regions can also be distinguished based on the behavior of the residual stresses; however, as follows from Figs. 5 and 6, region 2 is less pronounced, and in region 3, σ_y differs slightly in value from σ_x. In addition, with a sample thickness of 10 mm, positive (tensile) stresses in region 4 do not exceed 10 – 12 MPa, while with a sample thickness of 14 mm, they are approximately zero.

The stress profile in the non-annealed samples at a lower power density has the same features as in the annealed ones. When only the pulse density is decreased, a change in the profile and a decrease of

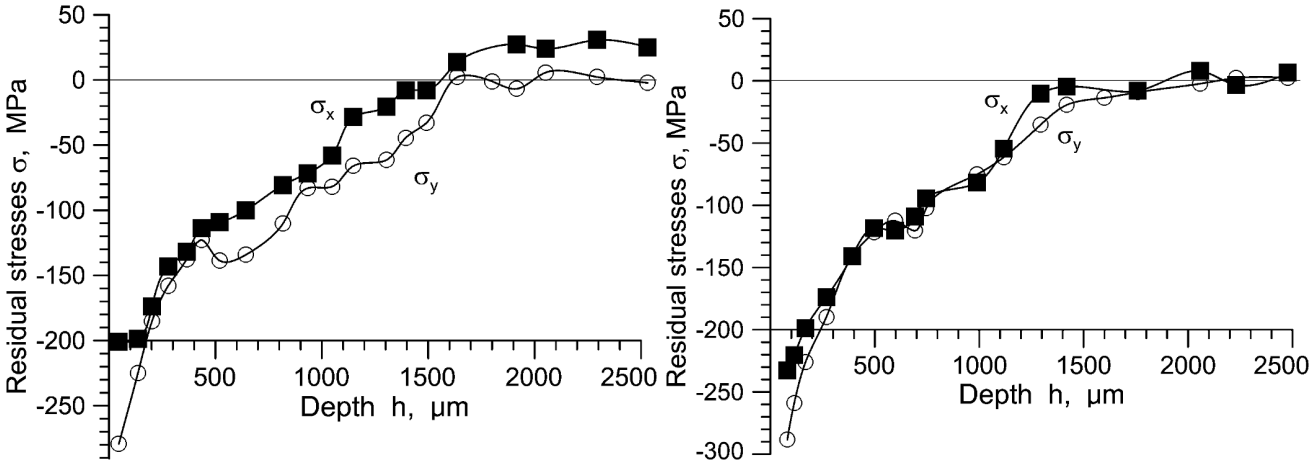

Fig. 6. Distribution of measured residual stresses σ_x (■) and σ_y (⊙) at $H = 14$ mm, $q = 4.4$ GW/cm^2, and $N = 2000$ pulses/cm^2 in original (left) and annealed (right) samples.

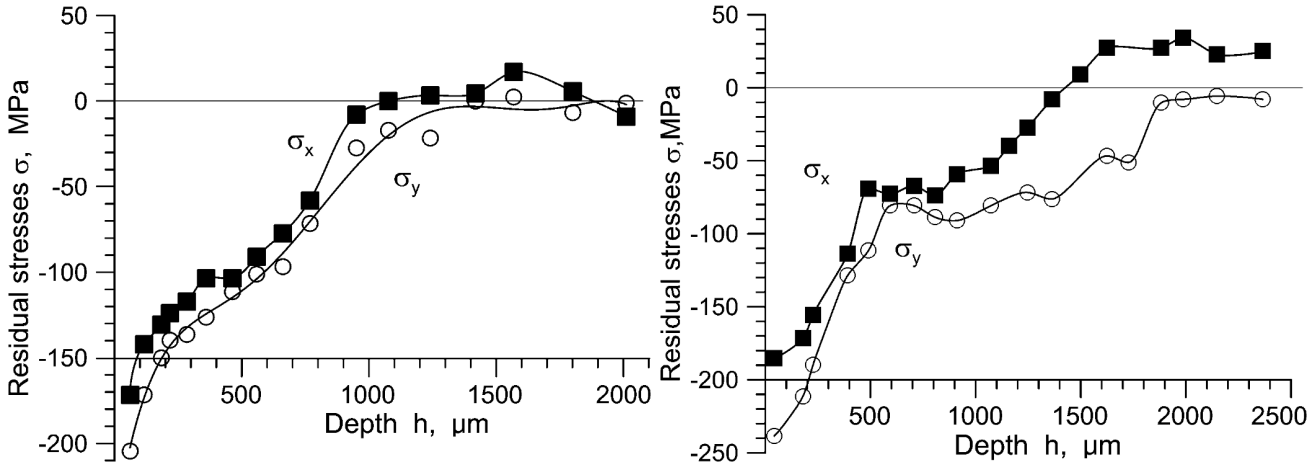

Fig. 7. Distribution of measured residual stresses σ_x (■) and σ_y (⊙) at different pulse densities; here, $H = 6$ mm and $q = 4.4$ GW/cm^2 at $N = 400$ pulses/cm^2 (left) and $N = 2000$ pulses/cm^2 (right).

tensile stresses are observed in region 4. In addition, homological distortions of the crystal lattice are significantly reduced. And though the CRS depth decreases (see Table 2 and Fig. 7), it remains large enough to select the optimum pulse density.

It should be noted that there are significant differences in the CRS profiles, their maximum values and depths in the AMg6 from the sheet samples studied in [19] and the AMg6 from the rod-shaped samples at $q = 1.1$ and 2 GW/cm^2. Thus, the residual stresses on the surface in the samples from the rod at $q = 2$ GW/cm^2 are approximately equal to the stresses in the AMg6 from the sheet samples, whereas at $q = 1.1$ GW/cm^2, their value is twice smaller, despite the difference in the pulse density. Moreover, even at $q = 4.4$ GW/cm^2 and $N = 2000$ pulses/cm^2, the depth σ_x is almost 1.5 times smaller; see Table 2. The noted difference is determined by two factors. First, different processing scheme was employed in [19], where the entire surface of the sample was processed. Second, there are differences in the structure of the materials studied, namely, the grain size, defect density, and crystallographic orientation of grains.

Determining the impact of each structural characteristic will be the subject of our upcoming studies.

When measuring residual stresses, we find that the width of the (511) line decreases with depth h, then, at a depth of $\approx 0.6\ h$, it starts to broaden with concurrent profile distortion. A further decrease in the linewidth occurs at depths greater than the CRS depth. Distortion of the (511) line for the non-annealed samples appears as asymmetry and emergence of a "hump" in the region of smaller angles; in the annealed samples line splitting may occur; see Fig. 8.

The most pronounced distortions of the (511) line are observed for the samples having a thickness of up to 8 mm. Such a behavior of diffraction lines can be due to homological distortions of the crystal lattice [22, 23] under the effect of residual stresses since maximum distortions occur in the layers with most different σ_x and σ_y at the boundary of the transition between compressive and tensile stresses; see Fig. 5. Significant homological distortions in the samples with a thickness smaller than 8 mm, along with the impact of the reflected shock wave, are likely the reason for the differences in the σ_x and σ_y profiles.

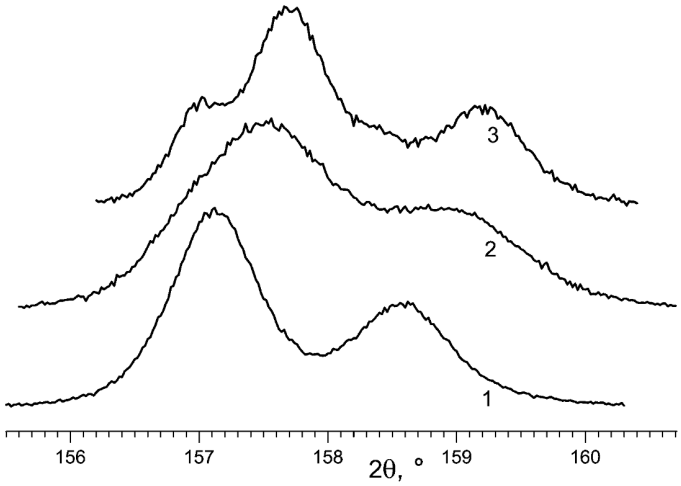

Fig. 8. Change in the profile of the (511) line with depth; here, line for an non-annealed sample without distortion (1), distortion of the line for the non-annealed sample (2), and distortion of the line for the annealed sample (3).

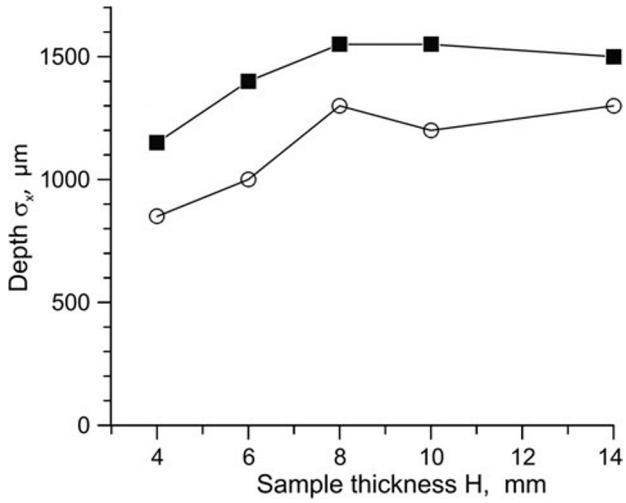

Fig. 9. Dependence of maximum depth σ_x on the sample thickness at $q = 4.4$ GW/cm^2 and $N = 2000$ pulses/cm^2 in original (■) and annealed (⊙) samples.

The thickness of the processed material obviously affects the CRS depth. In Fig. 9, we show the depth, at which the compressive stresses σ_x become zero. The shallower CRS depth at thicknesses of up to 8 mm may be caused by homological distortions, as well as by the effect of the reflected wave, which leads to tensile stresses, or a combination of these factors. The impact of the reflected wave can be enhanced by the Bauschinger effect, which is noticeably manifested at small deformations (up to 1%).

The difference in the CRS depth for the annealed and non-annealed material is determined, in our opinion, by differences in the material structure, including the crystallographic orientation of grains; see Fig. 3. In the FCC structures, sliding of edge dislocations occurs in the planes of the {111} system; therefore, the preferential orientation of any planes along the compression direction can lead to different results with respect to the formation of residual stresses.

In our experiments, the formation of significant CRS (up to −100 MPa) on the back side of the samples is established. For $H = 4 - 10$ mm, the magnitude of these stresses is almost independent of the material thickness, but depends on its structural state; see Table 3. Removal of the processed layer

in the annealed samples by electrolytic polishing leads to reduction of the stresses on the back side to the values close to values – characteristic of the original sample. For the non-annealed samples, a similar polishing procedure reduces residual stresses on the back side by a factor of approximately 2. Likely, the stresses on the back side of the annealed samples are due to the presence of an upper stressed layer, and they are almost completely elastic, whereas similar stresses in the non-annealed samples are only partially elastic, being partially caused by plastic deformation of the surface layer on the back side, as a result of the shock wave action.

Table 3. CRS Magnitudes on the Back Surface of AMg6.

q, GW/cm^2	N, pulses/cm^2	H, mm	σ_x/σ_y, MPa annealed	σ_x/σ_y, MPa original
4.4	2000	4	-41 / -49	-102 / -83
4.4	2000	8	-56 / -40	-92 / -80
4.4	2000	10	-56 / -40	-94 / -90

Increase in the number of processing cycles leads to a significant increase in the residual stresses, especially for the material having a thickness of up to 8 mm; specifically, they are increased by up to 20% with double surface processing. In this case, the stresses on the back side, which is not processed, are increased by a factor of 1.5. Bilateral processing, that is, sequential processing of both sides of the samples in mutually perpendicular or parallel directions, leads to increase in the CRS by up to 25% on the first side, depending on the direction; see Table 4.

Table 4. CRS Magnitudes on the Surface of AMg6 after Single and Double Bilateral Processing.

q, GW/cm^2	N, pulses/cm^2	H, mm	processing type	σ_x/σ_y, MPa;
4.4	2000	6	single	-185 / -239
			double	-224 / -253
4.4	2000	6	bilateral	-200 / -236
			perpendicular	-250 / -277
4.4	2000	6	bilateral	-195 / -262
			parallel	-237/ -293

It should be noted that double processing of one side is very similar to processing with a doubled pulse density, which, according to the results given in Table 2, does lead to increase in the stresses on the surface, whereas with bilateral LSPwC, processing of the back side leads to the appearance of additional induced stresses on the front side of the sample. The results on the depth distribution of dislocation density and residual stresses at multi-cycle and bilateral processing will be presented in the upcoming studies.

4. Conclusions

We considered the effect of laser shock peening without coating with low-energy pulses ($0.3 - 0.4$ J) on the structure and stress state of an AMg6 deformable Aluminum alloy with a thickness of 4 to 14 mm before and after recrystallization annealing. It was established that after LSPwC,

- roughness parameters Ra and Rz depended on the power density, processing step and were almost independent of preliminary heat treatment and initial roughness;
- maximum magnitude, depth, and profile of compressive residual stresses correlated with the characteristics of the crystal structure of the plastic deformation region and depended on the power density, pulse density, material thickness, and preliminary heat treatment;
- homological distortions of the crystal lattice were discovered in the region of compressive residual stresses, which were most pronounced at the boundary of the transition between compressive and tensile stresses.
- the formation of significant (up to -100 MPa) residual stresses on the unprocessed side of the non-annealed samples was observed. The magnitudes of compressive residual stresses on the back side of the annealed samples were $1.5 - 2$ times smaller.

Apart from the effect of the laser exposure parameters, the observed features of the distribution of dislocations and residual stress profiles at LSPwC can be due to the effect of the already processed material on the plastic deformations of the subsequently processed regions, differences in the material structure, as well as due to the effect of shock waves reflected from the back side of the sample on the structure.

References

1. A. H. Clauer, *Metals*, **9**, 626 (2019); DOI: 10.3390/met9060626
2. R. Sundar, P. Ganesh, R. K. Gupta, et al., *Lasers Manuf. Mater. Process.*, **6**, 424 (2019); DOI: 10.1007/s40516-019-00098-8
3. Y. Sano, K. Akita, K. Masaki, et al., *J. Laser Micro/Nanoeng.*, **3**, 161 (2006); DOI: 10.2961/jlmn.2006.03.0002
4. D. Karthik and S. Swaroop, *Mater. Manuf. Process.*, **32**, 1565 (2017); DOI: 10.1080/10426914.2016.1221095
5. S. Kalainathan and S. Prabhakaran, *Opt. Laser Technol.*, **81**, 137 (2016); DOI: 10.1016/j.optlastec.2016.02.007
6. E. Maawad, H.-G. Brokmeier, L. Wagner, et al., *Surf. Coat. Technol.*, **205**, 3644 (2011); DOI: 10.1016/j.surfcoat.2011.01.001
7. U. Trdan, J. A. Porro, J. L. Ocaña, and J. Grum, *Surf. Coat. Technol.*, **208**, 109 (2012); DOI: 10.1016/j.surfcoat.2012.08.048
8. J. Zhu, X. Jiao, C. Zhou, and H. Gao, *Energy Procedia*, **16A**, 153 (2012); DOI: 10.1016/j.egypro.2012.01.026
9. S. Sathyajith, S. Kalainathan, and S. Swaroop, *Opt. Laser Technol.*, **45**, 389 (2013)); DOI: 10.1016/j.optlastec.2012.06.019
10. K. Y. Luo, T. Lin, F. Z. Dai, et al., *Surf. Coat. Technol.*, **266**, 49 (2015); DOI: 10.1016/j.surfcoat.2015.02.017
11. X. Luo, Y. Zhang, K. Chen, and X. Ren, *Int. J. Microstruct. Mater. Prop.*, **8**, 53 (2013); DOI: 10.1504/IJMMP.2013.052646
12. U. Trdan, M. Skarba, and J. Grum, *Mater. Charact.*, **97**, 57 (2014); DOI: 10.1016/j.matchar.2014.08.020
13. U. Sánchez-Santana, C. Rubio-González, G. Gomez-Rosas, et al., *Wear*, **260**, 847 (2006); DOI: 10.1016/j.wear.2005.04.014

14. E. Maawad, Y. Sano, L. Wagner, et al., , *Mater. Sci. Eng. A*, **536**, 82 (2012); DOI: 10.1016/j.msea.2011.12.072
15. S. Prabhakaran and S. Kalainathan, *Mater. Des.*, **107**, 98 (2016); DOI: 10.1016/j.matdes.2016.06.026
16. Y. Sano, *Metals*, **10**, 152 (2020); DOI: 10.3390/met10010152
17. U. Trdan and J. Grum, *Adv. Mater. Sci. Eng.*, **16**, 1 (2015); DOI: 10.1155/2015/705306
18. I. A. Bakulin, N. G. Kakovkina, S. I. Kuznetsov, et al., *Inorg. Mater. Appl. Res.*, **12**, 55 (2021); DOI: 10.1134/S2075113321010032
19. I. A. Bakulin, S. I. Kuznetsov, A. S. Panin, and E. Yu. Tarasova, *Inorg. Mater. Appl. Res.*, **13**, 619 (2022); DOI: 10.1134/S2075113322030054
20. M. A. Attolico, C. Barile, C. Casavola, et al., *J. Mater. Eng. Perform.*, **31**, 7973 (2022); DOI: 10.1007/s11665-022-06857-7
21. M. Wang, C. Wang, X. Tao, and Y. Zhou, *Materials*, **15**, 7925 (2022); DOI: 10.3390/ma15207051
22. V. I. Mikheev, *Gomologiya kristallov*, Gostoptechizdat, Leningrad (1961) [in Russian].
23. E. Yu. Tarasova and S. I. Kuznetsov, *Bull. Leb. Phys. Inst.*, **35**, 291 (2008); DOI: 10.3103/S1068335608100011